Modelling and Simulation in Materials Science and Engineering

Surface energies and relaxation of NiCoCr and NiFe*X* (*X* = Cu, Co or Cr) equiatomic multiprincipal element alloys from first principles calculations

To cite this article: Wei Li *et al* 2022 *Modelling Simul. Mater. Sci. Eng.* **30** 025001

IOP Publishing Modelling and Simulation in Materials Science and Engineering

Modelling Simul. Mater. Sci. Eng. **30** (2022) 025001 (25pp) https://doi.org/10.1088/1361-651X/ac3e07

Surface energies and relaxation of NiCoCr and NiFe*X* (*X* = Cu, Co or Cr) equiatomic multiprincipal element alloys from first principles calculations

Wei Li[1,*], Xianghe Peng[1], Alfonso H W Ngan[2] and Jaafar A El-Awady[3]

[1] Department of Engineering Mechanics, Chongqing University, Chongqing 400044, People's Republic of China
[2] Department of Mechanical Engineering, The University of Hong Kong, Pokfulam Road, Hong Kong, People's Republic of China
[3] Department of Mechanical Engineering, Whiting School of Engineering, The Johns Hopkins University, Baltimore, MD 21218, United States of America

E-mail: weili0807@cqu.edu.cn and xhpeng@cqu.edu.cn

Received 27 July 2021, revised 19 November 2021
Accepted for publication 29 November 2021
Published 16 December 2021

Abstract

First principles calculations of the energies and relaxation of unreconstructed low-index surfaces, i.e. (001), (011) and (111) surfaces, in NiCoCr and NiFe*X* (*X* = Cu, Co or Cr) equiatomic multi-principal element alloys (MPEAs) are presented. The calculations were conducted for 12-layer slabs represented by special quasi-random supercells using the projector augmented wave method within the generalized gradient approximation. While experimental predictions are unavailable for comparison, the calculated surface energies agree fairly well with those from thermodynamic modeling and a bond-cutting model. In addition, the calculations unveil an important surface structure, namely, that the topmost surface layer is in contraction except for the (001) surface of NiFeCr alloy, the next layer below is in extension, and the bulk spacing is gradually recovered from the subsequent layers down. Additionally, the surface contraction is the most pronounced on the (011) plane, being about 4%–10% relative to the bulk spacings. The results presented here can provide an understanding of surface-controlled phenomena such as corrosion, catalytic activities and fracture properties in these equiatomic MPEAs.

*Author to whom any correspondence should be addressed.

Keywords: high entropy alloys, surface energy, surface relaxation, first principles calculations, thermodynamic modeling

(Some figures may appear in colour only in the online journal)

1. Introduction

Equiatomic multi-principal element alloys (MPEAs) [1, 2], where all constituent alloying elements have similar atom fraction are a special class of multicomponent alloy system. The reported outstanding mechanical properties (e.g. high strength, hardness and fracture toughness) of MPEAs over a wide range of temperatures [3] make them of particular interest for many applications in the aerospace, defense and nuclear power industries. Additionally, the compositional complexity of MPEAs has also lead to an increasing interest for corrosion [4, 5] and catalytic [6, 7] applications; for example, thin films of MPEAs have been studied as coating [8] and oxygen-reduction-reaction materials [6].

Surface energy, the excess free energy per unit area when a crystal is split along a specified crystalline plane into two new surfaces [9, 10], is one of the crucial material constants for understanding corrosion and catalytic activity as well as the fracture property of materials. Additionally, multicomponent alloys can exhibit numerous configurations and types of surface sites, and thus their surface energies may be different from those of their base metals. While the surface energies of numerous elemental metals have been reported [11], those for MPEAs are largely unknown with a few exceptions.

The surface energy is also fundamentally important in surface physics of materials. However, direct measurement of the surface energy through experiments is difficult, owing to the fact that experiments are usually conducted at the melting temperature to measure surface tension, which is then extrapolated to obtain the surface energy at zero temperature [12]. In addition, accurate surface energies of specific crystalline facets cannot be directly determined from such experiments. Therefore, theoretical calculation, which is much more accessible, has been an important tool for determining the surface energies of solids.

First principles calculations based on the density functional theory (DFT) have been extensively used to estimate the surface energies of elemental metals [10, 11], binary alloys [13], as well as MPEAs [14–16] and compounds [17, 18]. Vitos *et al* [11] used the linear muffin-tin orbital method within the full charge-density scheme (FCD-LMTO) to investigate the anisotropy of surface energies and establish a database of low index surface energies for 60 elemental metals in the periodic table, while Singh-Miller and Marzari [10] used the projector augmented wave pseudopotential method within the generalized gradient approximation (PAW-GGA) to study the relaxation, surface energies and work functions of low index surfaces of some elemental metals. Holec and Mayrhofer [17] and Zhang and Wang [18] also used the PAW-GGA method to calculate the surface energies of binary and ternary compounds. For MPEAs, Osei-Agyemang and Balasubramanian [14] calculated the (001) surface energy of a particular $Mo_{0.425}W_{0.425}Ta_{0.1}(TiZr)_{0.05}$ refractory high entropy alloy (RHEA) using DFT calculations within the PAW-GGA scheme. Li *et al* [16] obtained the surface energies of all low-index surfaces in the Hf–Nb–Ti–Zr–V–Ta–W RHEA system using DFT calculations based on the FCD exact muffin-tin orbital method within the local-density approximation, but the local lattice relaxation in these alloys cannot be reproduced with such a scheme.

In order to include the effects from lattice distortion in MPEAs, in the present work, we employ the PAW-GGA scheme to predict the surface energies and relaxation of low-index surfaces, i.e. (001), (011) and (111) surfaces, in ternary equiatomic MPEAs, i.e. NiCoCr,

NiCoFe, NiFeCr and NiFeCu alloys. Furthermore, we directly calculate the surface tension based on thermodynamics database and then extrapolate the calculated surface tension in the liquid phase to estimate the surface energy in the solid phase for the alloys studied.

The rest of the paper is organized as follows. In section 2, first the simulation method used to generate special quasi-random structure (SQS) simulation slabs with the interested orientations is described, and then the details of the DFT calculations and thermodynamics modeling are given. In section 3 the DFT predictions of the surface energies and surface relaxation of (001), (011) and (111) crystalline planes in the alloys considered are presented and compared with the surface energies predicted from thermodynamics modeling and the bond-cutting method (BCM). Finally, the summary and conclusions are given in section 4.

2. Methodology

2.1. Generation of SQS simulation slabs with different orientations

For bulk property calculations for an ordered structure, DFT calculations would involve periodic boundary conditions applied to a primitive or unit cell comprised of a few atoms. However, the alloys in the present study are complexly concentrated and entirely disordered on the long range, and for such random solid-solution alloys the notion of having periodic image atoms in a primitive cell that is small enough for DFT calculations would not be valid. On the other hand, a large supercell with a vast number of atoms would not be feasible due to the computational cost associated with such a large supercell. Alternatively, the SQS supercell [19] with a small unit cell consisting of dozens to hundreds of atoms, which has been successfully applied to high entropy alloys [20–22], is more feasible for a given random solid solution alloy.

For an SQS supercell, the correlation functions of the first few nearest neighbor shells match that of a target random alloy. Thereby we employed a Monte Carlo method, namely, the *mcsqs* code within the alloy theoretic automated toolkit (ATAT) developed by van de Walle *et al* [23], to generate the SQS supercells of the random solid solution alloys investigated. The pair correlation functions of an SQS supercell match, with some constrains, that of a random alloy up to the third-nearest neighbor [24]. To calculate the surface energies for special crystallographic planes of a face-centred cubic (fcc) crystal, e.g. the {001}, {011} and {111} planes, cubic SQS supercells with special crystallographic orientations need to be constructed, however, the SQS cell generated through the *mcsqs* code does not usually remain cubic if no additional operations are performed [25]. As such, it is necessary to control the orientation and shape of the SQS supercell by specifying the appropriate lattice vectors and dimensions of the cell in the rndstr.in and sqscell.out files of the ATAT, respectively.

Three fcc SQS supercells consisting of 12 layers of atoms with: {001} planes perpendicular to x, y and z axes, respectively; {011} plane parallel to the x–y plane; and {111} plane perpendicular to the z axis, are produced using the lattice vectors listed in table 1. In this case, the three vectors in the sqscell.out file determine the dimensions in the x, y and z directions of a cubic cell respectively. Meanwhile, to maintain the periodicity in the x, y and z directions of the supercell, the dimensions in y and z directions should be multiples of $a/\sqrt{2}$, $\sqrt{3/2}a$ and $\sqrt{3}a$, respectively for the three cells listed in table 1, where a is the mean lattice constant of the alloy. It should be noted that the SQS for each alloy is not unique. Hence, to take the effect of random distribution of atoms into consideration, five SQS supercells with different random structures were constructed to represent every alloy and every surface studied here. By comparing with calculations with a larger system and more independent SQS supercells, (see appendix), the abovementioned system and supercell number were found to be sufficient to eliminate significant effects due to system size and randomness.

Table 1. Input control parameters for the 12-layer fcc SQS supercells having three different special crystallographic orientations. The lattice vectors and cell dimensions are given in Cartesian coordinates in units of a, the lattice constant.

	$SQS_{\{001\}}$	$SQS_{\{011\}}$	$SQS_{\{111\}}$
Lattice vectors	(0.0, 0.5, 0.5)	(0.0, 0.7071, 0.0)	(−0.3536, 0.6124, 0.0)
	(0.5, 0.0, 0.5)	(0.5, 0.3536, 0.3536)	(0.3536, 0.6124, 0.0)
	(0.5, 0.5, 0.0)	(0.5, 0.3536, −0.3536)	(0.0, 0.4082, −0.5774)
Cell	(2.0, 0.0, 0.0)	(2.0, 0.0, 0.0)	(1.414, 0.0, 0.0)
(x, y, z)	(0.0, 2.0, 0.0)	(0.0, 2.828, 0.0)	(0.0, 2.449, 0.0)
Dimensions	(0.0, 0.0, 6.0)	(0.0, 0.0, 4.2426)	(0.0, 0.0, 6.928)

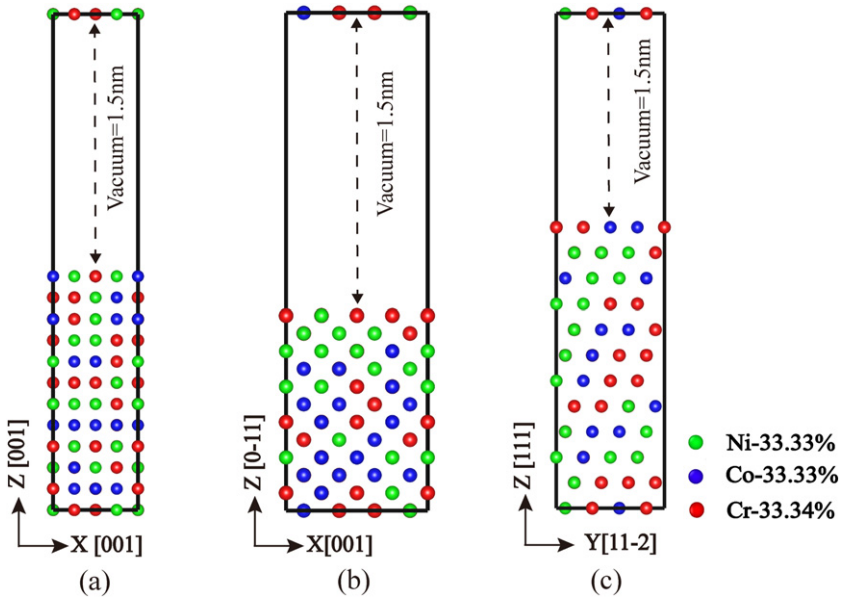

Figure 1. Schematic representations of the SQS slabs for a NiCoCr alloy with different surfaces parallel to the: (a) {001}; (b) {011}; and (c) {111} crystallographic planes.

The free surfaces were introduced by inserting a vacuum region next to the desired crystallographic plane into the SQS supercell after complete ionic relaxation, thus forming a crystal/vacuum slab in its periodic repetition, as shown schematically in figure 1. The thickness of the vacuum region is 15 Å to prevent unphysical interactions between two adjacent replicated slabs, so that the surface behavior would mimic that in an infinitely thick vacuum region [14]. In addition, choosing the slab of 12 atomic layers provides sufficient atomic layers so that the top and bottom surface layers of atoms are well separated to minimize the internal interactions between bulk and surface atoms.

2.2. DFT calculations

All DFT calculations here were performed using the Vienna *ab initio* simulation package (VASP) [26, 27] with GPU-accelerated port [28, 29]. The interaction of core electrons and

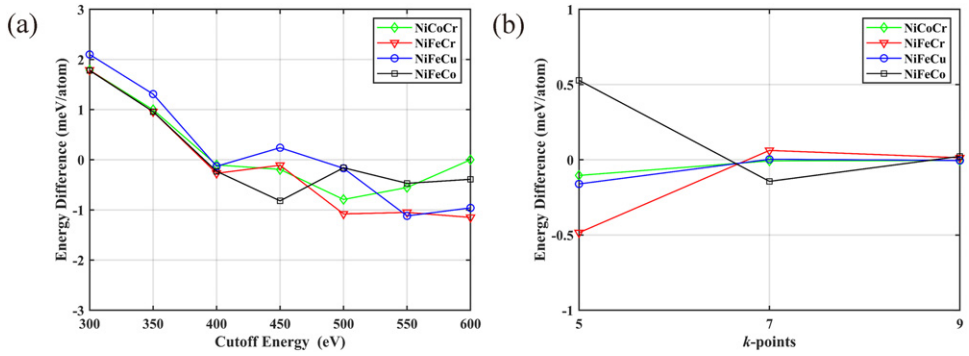

Figure 2. Convergence tests for the: (a) cutoff energies; and (b) *k*-points of the alloys investigated.

nuclei was represented by PAW pseudo-potentials [30], and the exchange–correlation interaction was described within GGA as simplified by the method of Perdew, Burke and Ernzerhof [31]. Within VASP-GPU, a mixture of the Davidson-block iteration scheme and RMM-DIIS algorithm was employed to conduct the electronic minimization, and the projection operators were evaluated in real space, which were optimized automatically. Additionally, the precision mode was set as 'accurate' throughout the calculations.

For the calculations involving alloys with multiple components, it is necessary to perform convergence tests on the input parameters before bulk and surface calculations are conducted. Thus, several calculations with different plane-wave cutoff energies and *k*-points using the SQS supercells with 48 atoms to represent the bulk alloys were performed. As shown in figure 2, the total energy calculated converges within 1 meV/atom [17, 32] beyond a cutoff energy of 350 eV and five *k*-points. Consequently, the cutoff energy was taken as 350 eV throughout the calculations, and Brillouin-zone integrations were performed using Gamma centered Monkhorst–Pack [33] *k*-point meshing scheme, with the *k*-point sampling set to $5 \times 5 \times 5$ and $5 \times 5 \times 1$ for bulk and surface calculations respectively of the studied alloys.

The Methfessel–Paxton scheme with a smearing width of 0.2 eV, and the tetrahedron method with Bloechl corrections, were employed during the total energy calculations for ionic relaxation and electronic static calculations, respectively. The convergence criteria were taken to be 1×10^{-4} eV and 0.02 eV $\mathrm{\AA}^{-1}$ [14] for electronic self-consistent calculations and ionic relaxations, respectively, throughout the calculations. Experiments and simulations have shown that there is severe lattice distortion in MPEAs [34, 35]; therefore we performed complete relaxation of the ionic positions with respect to both the volume and shape of the unit cell [18, 32, 36] using a conjugate-gradient algorithm once the SQS supercell was generated. During the surface energy calculation, conversely, we carried out selectively dynamic ionic relaxation without any change to the volume and shape of the unit cell. Furthermore, considering the computational expense and the need to keep the interaction between adjacent surfaces as small as possible, the surface relaxation was performed only on the top seven layers of atoms of the slab, while the rest of the atoms were fixed at their bulk positions [14]. As shown in the inset of figure 3, using NiCoCr alloy as an example, when the first three atomic layers are relaxed, the total energies of the simulated slabs converge within 1 meV/atom. Additionally, calculations with and without spin polarization were conducted to understand the effect of magnetism on the bulk and surface properties of the alloys considered. For comparison we

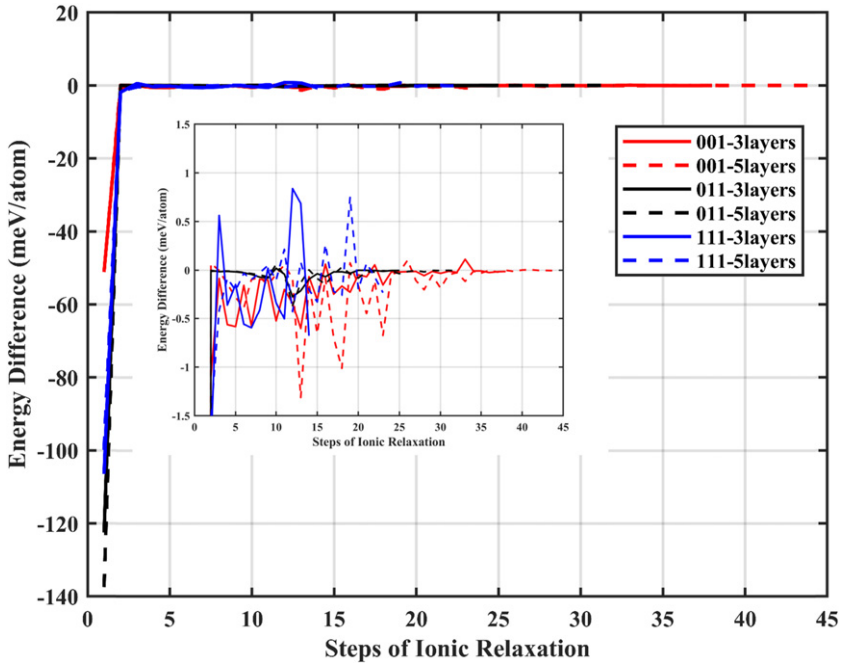

Figure 3. Convergence tests for different numbers of surface layers relaxed in NiCoCr alloy.

also calculated the relaxation within the top four and six atomic layers for the NiCoCr alloy, and the results are given in table A2.

2.3. Thermodynamic modeling

Theoretical calculations to estimate the surface energies of the alloys investigated were also conducted using thermodynamic modeling. Tyson *et al* proposed a semi-theoretical approach based on the surface tension in the liquid phase to estimate the surface energy in the solid phase as follows [12]:

$$\gamma_{\mathrm{SV}}^{T} = \alpha \cdot \gamma_{\mathrm{LV}}^{T_m} + \int_{T}^{T_m} \frac{S_{\mathrm{SV}}}{A}\,\mathrm{d}T, \tag{1}$$

where γ_{SV}^{T} denotes the solid-vapor interfacial energy at temperature T, $\gamma_{\mathrm{LV}}^{T_m}$ denotes the liquid-vapor interfacial energy at melting point, S_{SV} is surface entropy as a function of temperature, and A is the molar surface area given as:

$$A = cN^{1/3}V^{2/3}, \tag{2}$$

where N is Avogadro's number, V the molar volume, and c is 1.26, 1.78 and 1.09 for the $\{100\}$, $\{110\}$ and $\{111\}$ planes respectively [37]. In equation (1), α is the ratio of the solid–liquid interfacial energy and solid-vapor interfacial energy according to the following relationship:

$$\alpha = 1 + \frac{\gamma_{\mathrm{SL}}}{\gamma_{\mathrm{gb}}} \cdot \frac{\gamma_{\mathrm{gb}}}{\gamma_{\mathrm{SV}}}. \tag{3}$$

Here γ_{SL}/γ_{gb} is 0.45 [38] for all constituent elemental metals, $\gamma_{gb}/\gamma_{SV} = 1/3\sum(\frac{\gamma_{gb}}{\gamma_{SV}})_i$, where $(\frac{\gamma_{gb}}{\gamma_{SV}})_i$ is the ratio of the grain boundary energy and solid-vapor interfacial energy for the constituent elemental metals.

2.3.1. Surface tension of ternary alloys. According to equation (1), the surface tensions in the liquid phase, γ_{LV}, of the four alloys at the melting point must be computed first. Here, Butler's model, which has been extensively used to estimate the surface tension of binary and ternary alloys [39, 40], is employed to calculate the surface tensions of the considered alloys. The surface tension of ternary alloys in liquid phase is given by:

$$\gamma = \gamma_i + \frac{RT}{A_i}\ln\frac{X_i^s}{X_i^b} + \frac{1}{A_i}\left\{G_i^{ex,s}(T,X_j^s) - G_i^{ex,b}(T,X_j^b)\right\}, \tag{4}$$

where R, T, γ_i and A_i are gas constant, temperature, surface tension and molar surface area of pure component i, respectively, the subscripts i and j refer to the constituent elements of the alloy, and X_i^s and X_i^b are the molar fraction of component i in a surface and bulk composition, respectively.

2.3.2. Partial excess Gibbs free energy. In equation (4), $G_i^{ex,s}(T,X_j^s)$ and $G_i^{ex,b}(T,X_j^b)$ are the partial excess Gibbs free energy of component i in the surface and bulk composition, respectively, both are functions of temperature and concentration of the other two components and can be calculated with:

$$G_i^{ex,b} = G_{A-B-C}^{ex} + \sum_{j=2}^{3}\left(\delta_{ij} - X_j^b\right)\frac{\partial G^{ex}}{\partial X_j^b}, \tag{5}$$

where i and $j = 1$, 2 or 3, equivalent to element A, B or C, δ_{ij} is the Kronecker's delta, and G_{A-B-C}^{ex} is the excess Gibbs free energy due to mixing of the A, B and C elements for a liquid ternary alloy.

For partial excess Gibbs free energy of surface composition i, $G_i^{ex,s}$, Tanaka and Iida [40] proposed that $G_i^{ex,s}$ and $G_i^{ex,b}$ are proportional, i.e.

$$G_i^{ex,s}\left(T,X_j^s\right) = \beta G_i^{ex,b}\left(T,X_j^s\right), \tag{6}$$

where β is the ratio between the two coordination numbers (CNs) in the surface and bulk phase. For fcc alloys [41], β is usually taken as 0.75 [40, 42], and since the alloys investigated in this work are fcc crystals, the value of 0.75 was used in all the present thermodynamic calculations.

2.3.3. Excess Gibbs free energy of mixing based on the Muggianu model. With a subregular solution model, the excess Gibbs free energy of a ternary alloy in the liquid phase, the G_{A-B-C}^{ex} in equation (5), is described by the Muggianu model in the form of Redlich–Kister polynomials [43] as:

$$G_{A-B-C}^{ex} = \sum_{i\neq j} X_i^b X_j^b \sum_{v=0}^{n} L_{ij}^v\left(X_i^b - X_j^b\right)^v, \tag{7}$$

where $i, j = A, B$ or C and $i \neq j$, L_{ij}^v is the interaction energy of the constituent binary subsystems as listed in table 2, which depends only on temperature but not on concentration. As ternary interactions are much smaller than binary interaction [42], in equation (7) the term $X_A^b X_B^b X_C^b L_{ABC}$ is neglected.

Table 2. Interaction parameters of the constituent binary subsystems, L^{v}_{ij}.

Subsystem	L^{0}_{ij} (J mol^{-1})	L^{1}_{ij} (J mol^{-1})	References
Fe–Ni	$-18380 + 6.04T$	$9228 - 3.55T$	[43]
Cu–Fe	$36\,088 - 2.33T$	$324.53 - 0.033T$	[43]
Cu–Ni	$11\,760 + 1.084T$	-1672	[43]
Co–Cr	$-12008.6239 + 2.2019T$	$-5836.4696 + 1.1402T$	[42]
Fe–Co	-9312	-1752	[44]
Fe–Cr	$-5.257T$	-5419.8	[45]
Cr–Ni	$318 - 7.33T$	$16\,941 - 6.37T$	[42]
Co–Ni	1331	0	[42]

2.3.4. Excess Gibbs free energy of mixing based on Chou's model. Another model, known as Chou's general solution model, has also been proposed to cover the features of both symmetric and asymmetric models [46, 47]. According to this model, the excess Gibbs free energy of a ternary alloy in the liquid phase is given as:

$$G^{\mathrm{ex}}_{A-B-C} = \sum_{i\neq j} X^{b}_{i} X^{b}_{j} \sum_{v=0}^{n} L^{v}_{ij} \left(X^{b}_{i} - X^{b}_{j} + (2\varepsilon_{ij} - 1)X^{b}_{k}\right)^{v}, \tag{8}$$

where ε_{ij} is the similarity coefficient defined as:

$$\varepsilon_{ij,i\neq j} = \frac{\eta_i}{\eta_i + \eta_j}, \tag{9}$$

and then the deviation sum of squares η_i is calculated as:

$$\eta_i = \frac{1}{30}\left(L^{0}_{ij} - L^{0}_{ik}\right)^{2} + \frac{1}{210}\left(L^{1}_{ij} - L^{1}_{ik}\right)^{2}. \tag{10}$$

2.3.5. Surface concentration. To obtain the surface tension of the ternary alloys, the surface composition, X^{s}_{i}, in equation (4) needs to be calculated. Egry *et al* [48] proposed a simple model, through defining an average metal in a quasi-binary system, to calculate the surface concentration as:

$$X^{s}_{i} = \frac{X^{b}_{i}}{X^{b}_{i} + \left(1 - X^{b}_{i}\right)\exp\left[S_A\left(\gamma_{i-}\gamma_{jk}\right)/T\right]}, \tag{11}$$

where $\exp\left[S_A\left(\gamma_{i-}\gamma_{jk}\right)/T\right]$ is the surface segregation factor, $S_A = 1.09N^{1/3}V^{2/3}/R$, γ_{jk} is the surface tension of the average metal j–k in the quasi-binary system, which is taken as $\gamma_{jk} = 0.5(\gamma_j + \gamma_k)$ in the present work.

3. Results and discussions

3.1. Bulk properties

Before investigating the surface energies, bulk properties including lattice constants, bulk moduli and cohesive energies of the alloys (i.e. NiCoCr, NiCoFe, NiFeCr and NiFeCu) and their constituent elemental metals were first calculated. The bulk properties of the constituent elemental metals were first calculated, whereas Fe, Cr and Co metals with fcc lattice were also

Table 3. Lattice constant (a), bulk modulus (B) and cohesive energy (E_{coh}) of the constitute elemental metals of the alloys considered here from DFT calculations, in comparison with experiments and previous DFT calculations reported in literature. All present calculations were performed with spin polarization. For the hcp lattice, c/a ratios are listed.

	a (Å)			B (GPa)			E_{coh} (eV/atom)		
	Pres.	Prev.	Expt.	Pres.	Prev.	Expt.	Pres.	Prev.	Expt.
Ni	3.515	3.506[a]	3.52[b]	195	194[c]	185[d]	4.84	4.78[ce]	4.45[f]
Cu	3.635	3.631[a]	3.61[b]	139	—	137[b]	3.49	3.50[a]	3.52[f]
Fe_{-fcc}	3.476	3.504[a]	—	152	164[a]	—	4.95	—	—
Fe_{-bcc}	2.833	2.832[a]	2.853[g]	178	174[h]	168[b]	5.11	4.89[a]	4.30[b]
Cr_{-fcc}	3.609	—	—	156	—	—	5.11	—	—
Cr_{-bcc}	2.835	2.855[h]	2.88[b]	260	255[i]	191[j]	5.51	4.55[i]	4.10[b]
Co_{-fcc}	3.538	3.518[k]	—	224	—	—	5.17	5.48[k]	
Co_{-hcp}	1.633		1.62[b]	207	—	191[b]	5.18	5.49[b]	4.39[b]

[a]Reference [50].
[b]Reference [51].
[c]Reference [13].
[d]Reference [52].
[e]Reference [53].
[f]Reference [54].
[g]Reference [55].
[h]Reference [56].
[i]Reference [57].
[j]Reference [58].
[k]Reference [59].

calculated because all alloys in this study have an fcc lattice structure. The volume-energy data were fitted with the third-order Birch–Murnaghan equation of state [49] to obtain the lattice constants and bulk moduli, and the cohesive energies of the metals were calculated as $E_{coh} = \{N \times E_{atom} - E_{bulk}\}/N$, where E_{bulk} is the total bulk energy of a simulation cell consisting of N identical atoms, and E_{atom} denotes the total energy of a single isolated constituent atom. Spin polarization was taken into consideration in the calculation for the elemental metals. The results are summarized in table 3, which shows excellent agreement between the present and previous calculations, as well as experimental values.

It is worth noting that the calculations for the lattice constants of MPEAs is significantly different from that in elemental metals due to the severe distortion in MPEAs, i.e. the lattice constants are variable for MPEAs. Therefore, highly accurate prediction of the lattice constant and bulk modulus of MPEAs is a significant challenge. Thus, to compute the bulk properties of the alloys considered, SQS supercells were utilized, each consisting of 48 atoms. Initially, for each alloy, an SQS supercell with an undistorted fcc lattice was constructed; then the lattice constant of this supercell was varied within a range based on the mean of the lattice constants of the constituent elements to calculate the corresponding total energy, then, the energy-lattice constant data were fitted by the third-order Birch–Murnaghan equation of state to extract the equilibrium lattice constant and bulk modulus of the alloy with an undistorted lattice. The predicted values are listed in the fourth (Pris. M) and ninth columns of table 4, respectively. Furthermore, in order to reproduce the lattice distortion in an MPEA, thorough energetic minimization was performed, i.e. the atomic positions as well as the volume and shape of the supercell were allowed to change during the minimization, and the equilibrium lattice constant of the distorted supercell was determined by averaging the second nearest neighbor distances

(SNNDs); the results are shown in the second column (Dist. M) of table 4. In addition, to investigate the effect of magnetism, non-spin polarization calculations were also performed and the results are listed in third column (Dist. NM) of table 4. It is seen that the predicted lattice constant when including magnetism is larger than that without including magnetism, which agrees well with the experimental and calculated values reported previously.

The binding or cohesive energy was also calculated as $E_{\text{coh}} = \{\sum E_{\text{atom}} - E_{\text{bulk}}\}/N$, where E_{bulk} is the total bulk energy of the simulation cell, with or without relaxation, and listed in table 4. Based on the calculated cohesive energies of the constituent elemental metals and the alloy under investigation, the enthalpy of mixing of the alloy was then computed from $\Delta H_{\text{mix}} = E_{\text{coh}} - x_A E^A_{\text{coh}} - x_B E^B_{\text{coh}} - x_c E^C_{\text{coh}}$, where x_i are the molar fractions of the constituent elements A, B and C. As shown in table 4, the enthalpy of mixing of NiFeCo and NiFeCu alloys is nearly zero, while that of NiCoCr and NiFeCr alloys is positive, indicating that NiFeCo and NiFeCu alloys are nearly ideal solutions, while clustering would occur for the NiCoCr and NiFeCr alloys, which is consistent with experimental observations of NiCoCr [63].

3.2. Local relaxations due to lattice distortion

To quantitatively characterize the local relaxation in the solid solutions of NiCoCr, NiCoFe, NiFeCr and NiFeCu, the calculated SNNDs for each pair of atomic species in their relaxed SQS supercells are shown in figures 4(a)–(d). In each alloy, the horizontal dashed line represents the mean lattice constant and the filled squares denote the mean SNND for each pair of atomic species. It is shown that the SNND values for each pair of species exhibit a scattered distribution, in which some SNNDs are larger than the mean lattice constant of the alloy while others are smaller. For example, the mean SNND of Ni–Ni in the NiCoCr solid solution is 3.523 Å, which is larger than the 3.515 Å in the pure Ni. In contrast, the mean SNNDs of Co–Co and Cr–Cr in the NiCoCr solid solution are 3.526 and 3.529 Å, which are smaller than the 3.538 and 3.609 Å in pure fcc Co and fcc Cr, respectively. As shown in table 5, similar extension and contraction in like-atom SNNDs also occur in the other solid solutions except for the case of the NiCoFe alloy, where all like-atom SNNDs exhibit extension. Although all like-atom SNNDs in NiCoFe are in extension, the mean SNNDs for unlike-atoms in all alloys studied here show larger or smaller values in comparison with the mean lattice constant of the alloy, indicating that their lattices are all distorted with a variation in the bond length.

3.3. Surface energies from BCM

The simplest and the most intuitive estimate for the surface energy is that given in the BCM [64, 65], i.e. the surface energy is the product of the bonding energy and the number of bonds broken when a new surface is introduced. Within the tight-binding theory and second-moment approximation the surface energy is proportional to the square root of the CNs as:

$$\gamma = \left(1 - \frac{\sqrt{Z_S}}{\sqrt{Z_B}}\right) E_{\text{coh}}, \tag{12}$$

where Z_S and Z_B are the CNs of atoms on the topmost atomic layer and in the bulk lattice, respectively. Within the quasi-chemical scheme only the first nearest neighbors are taken into account to calculate the total energy of surface atoms in equation (12). However, Mezey and Giber [66] noted that the contribution from the second nearest neighbors should be included, and introduced the effective CNs $\overline{Z}_S$ and $\overline{Z}_B$ to replace Z_S and Z_B in equation (12), the effective CNs being the sum of the CN for the first nearest neighbors and half of the CN for the second nearest neighbors. In the FCC structure, $\overline{Z}_B$ is therefore $12 + 0.5 \times 6 = 15$, and the $\overline{Z}_S$ for the (100), (110) and (111) surface is 10.5, 9 and 10.5, respectively [66]. Here, we employ the BCM

Table 4. The lattice constant (a), bulk modulus (B), cohesive energy (E_{coh}), and mixing enthalpy (ΔH_{mix}) as predicted from the current DFT calculations for the considered alloys. Available predictions in literature from experiments and previous DFT calculations are also listed for comparison. 'Dist.' and 'Pris.' refer to the lattices with and without distortion, respectively, while 'M' and 'NM' denote the calculations with and without spin polarization respectively.

	a (Å)							B (GPa)		E_{coh} (eV/atom)		ΔH_{mix} (eV/atom)	
Comp.	Dist. M	Dist. NM	Pris. M	Dist. M[a]	Dist. NM[a]	Pris. M[a]	Expt.	Pris.M	Expt.	Dist. M	Pris.M	Dist. M	Pris. M
NiCoCr	3.519	3.511	3.523	—	3.515	—	3.559[b]	210	187[b]	5.09	5.07	0.053	0.034
NiFeCo	3.541	3.464	3.497	3.547	3.468	3.552	3.557[c]	195	177[b]	4.99	4.93	0.008	−0.059
NiFeCr	3.551	3.512	3.524	3.544	3.516	3.547	3.589[c]	267	—	5.07	5.05	0.100	0.080
NiFeCu	3.583	3.530	3.588	—	—	—	3.555[d]	168	—	4.43	4.42	0.002	0.0003

[a]Reference [32].
[b]Reference [60].
[c]Reference [61].
[d]Reference [62].

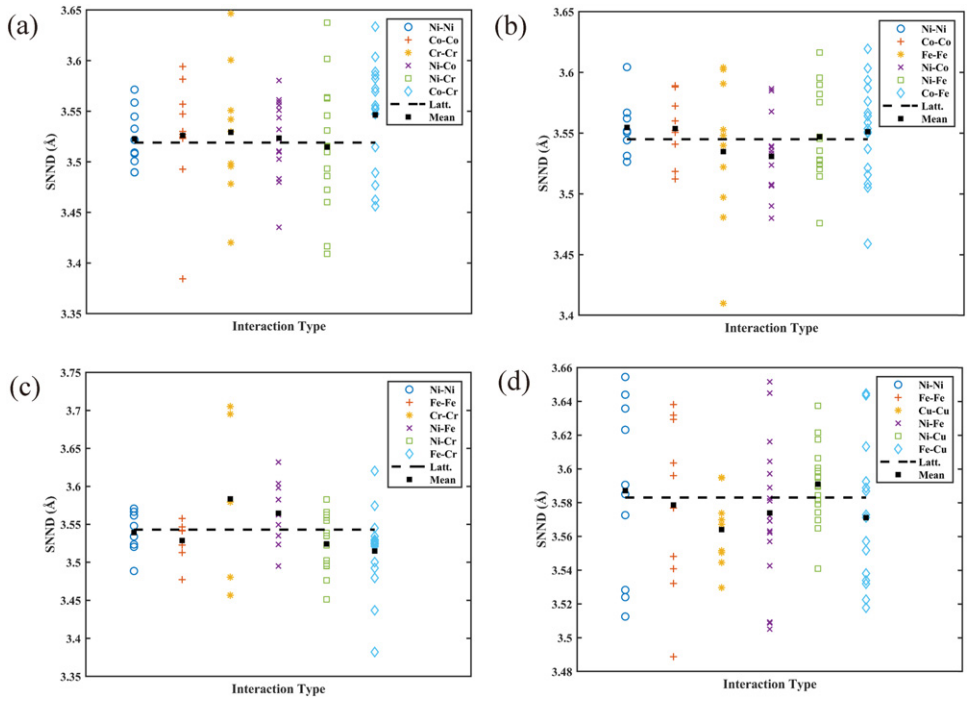

Figure 4. SNND distributions for: (a) NiCoCr; (b) NiCoFe; (c) NiFeCr; and (d) NiFeCu alloys.

Table 5. The SNNDs (Å) of i–i atomic pairs in the different alloys considered. Positive signs indicate bond extension, i.e. the SNND in a solid solution is larger than that in the corresponding element, and vice versa.

Interaction type	NiCoCr	NiCoFe	NiFeCr	NiFeCu
Ni–Ni	3.523(+)	3.555(+)	3.539(+)	3.587(+)
Co–Co	3.526(−)	3.554(+)	—	—
Cr–Cr	3.529(−)	—	3.583(−)	—
Fe–Fe	—	3.535(+)	3.529(+)	3.579(+)
Cu–Cu	—	—	—	3.564(−)

model based on effective CNs and the calculated cohesive energies as given in table 4 to estimate the surface energies of the alloys considered. The results are listed in table 6 and shown in figures 5(a)–(c) in which the four alloys are listed on the horizontal axis in an increasing sequence based on their DFT-calculated surface energies, which is also the sequence of increasing cohesive energy. It is observed that for all three (001), (011) and (111) surfaces, the surface energy estimated from the BCM roughly follows an increasing trend with the cohesive energy of the alloys considered here as listed in table 4. Moreover, in terms of the detailed quantities, there is good agreement between the predictions from the BCM and the DFT calculations only for the (001) surface of NiCoFe and NiFeCu alloy as shown in figure 5(a), (011) surfaces of the NiFeCr and NiCoCr alloys as shown in figure 5(b), and (111) surface of the NiFeCu and NiCoFe alloys as shown in figure 5(c). On the other hand, the poor agreement between the

Table 6. Surface energies of the alloys investigated here as predicted from DFT calculations and estimated based on thermodynamics modeling and BCM.

		γ_{BCM} (J m^{-2})			γ_{RKC} (J m^{-2})			γ_{RKM} (J m^{-2})			$\gamma_{DFT\text{-}unrelaxed}$ (J m^{-2})			$\gamma_{DFT\text{-}relaxed}$ (J m^{-2})		
Comp.	T (K)	(001)	(011)	(111)	(001)	(011)	(111)	(001)	(011)	(111)	(001)	(011)	(111)	(001)	(011)	(111)
NiCoCr	0	2.000	2.761	2.000	2.486	2.503	2.001	2.483	2.499	1.998	2.632	2.650	2.393	2.552	2.553	2.231
NiFeCo	0	1.961	2.707	1.961	2.528	2.543	2.035	2.527	2.543	2.035	2.208	2.232	2.099	2.097	2.066	2.059
NiFeCr	0	1.991	2.748	1.991	2.473	2.482	2.012	2.473	2.481	2.025	2.619	2.642	2.463	2.484	2.525	2.343
NiFeCu	0	1.740	2.401	1.740	1.735	1.745	1.444	1.735	1.746	1.444	2.023	2.150	1.757	1.981	2.059	1.673

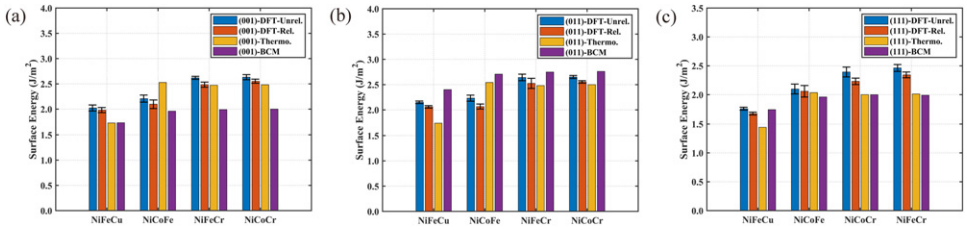

Figure 5. Surface energies for: (a) (001); (b) (011); and (c) (111) surfaces, of the alloys investigated here as predicted from DFT calculations and estimated based on thermodynamics modeling and BCM. The error bars in the DFT calculations represent the variations in the predictions from different random SQS supercells for each alloy.

Table 7. The excess Gibbs free energy of mixing $\left(G^{\text{ex}}_{A-B-C}\right)$ and surface tension (γ) of the alloys considered as predicted by the Muggianu's and Chou's models, which are denoted by subscripts M and C, respectively.

Comp.	$G^{\text{ex}}_{A-B-C,M}$ (J mol^{-1})	$G^{\text{ex}}_{A-B-C,C}$ (J mol^{-1})	γ_M (J m^{-2})	γ_C (J m^{-2})
NiCoCr	-2.177×10^3	-2.419×10^3	1.866	1.869
NiFeCo	-1.721×10^3	-1.753×10^3	1.897	1.897
NiFeCr	-3.389×10^3	-3.561×10^3	1.812	1.812
NiFeCu	4.233×10^3	4.294×10^3	1.236	1.235

BCM and the DFT calculations for all (011) surface energies can be explained by the absence of surface relaxation in BCM. Additionally, magnetic effects are also not incorporated in BCM [67], and repulsive forces are not included in the tight binding scheme. All of which can explain the discrepancies between the BCM predictions and the DFT calculations.

3.4. Surface tensions obtained from thermodynamics

Before estimating the surface energies of the alloys in the solid phase (i.e. 0 K) according to equation (1), the surface tensions at the melting point must be evaluated first. Thus, the excess Gibbs free energy of mixing based on Muggianu's and Chou's models is first calculated using equations (7) and (8), respectively, and the results from the two models are remarkably close as shown in table 7. Then, the partial excess Gibbs free energies of the constituent elements of the alloys are calculated based on equation (5), wherein the melting points of NiCoCr and NiFeCo alloys are 1690 K and 1724 K respectively [60], and those of NiFeCu and NiFeCr alloys were calculated from $T_m^{\text{alloy}} = \sum_i^n c_i(T_m)_i$ [68], where $(T_m)_i$ and c_i are the melting point and concentration of each constituent, and the surface concentrations, X_i^s, in equation (4) are calculated according to equation (11). Finally, the surface tensions of the alloys considered were calculated using Butler's model, i.e. based on equation (4) and the thermodynamic data for the constituent elements listed in table 8. The predictions of the surface tensions of the alloys based on the excess Gibbs free energy of mixing computed with the Muggianu and Chou models are shown to be in excellent agreement with each other.

3.5. Estimate of the surface energies based on surface tension

The change of surface entropy with temperature is the primary contribution to the temperature dependence of surface energies. Tyson and Miller [12] pointed out that the contributions of

Table 8. Thermodynamic data for the constituent elements for use with the Butler's model.

Metal	Tm[a] (K)	γ_{Tm} (N m^{-1})	d_r/d_T (10^{-3} N m^{-1} K^{-1})	S_A (K m N^{-1})	γ_{gb}/γ_{SV}[e]
Ni	1728	1.838[b]	0.42[b]	4219[c]	0.38
Fe	1811	1.915[c]	0.397[c]	4510[c]	0.37
Cu	1358	1.334[d]	0.26[d]	4528[c]	0.32
Co	1768	1.884[b]	0.37[b]	5000	0.36
Cr	2178	1.672[b]	0.20[b]	5000	0.42[f]

[a]Reference [69].
[b]Reference [42].
[c]Reference [39].
[d]Reference [43].
[e]Reference [12].
[f]Reference [70].

both vibrational and configurational entropy should be considered for more accurate prediction of surface energies at different temperatures. For metals, under the assumption of a linear variation, the vibrational entropy varies from zero at 0 K to $0.8R$ at $0.2T_m$, and the configurational entropy varies from zero at $0.5T_m$ to R at T_m [12]. Therefore, the second term of equation (1), $\int_T^{T_m} \frac{S_{SV}}{A}\,\mathrm{d}T$, equals $0.97T_mR/A$ when T is zero K. The surface energies at 0 K of low-index surfaces of the alloys estimated using equation (1) are summarized in table 6, which fairly agree with those obtained from DFT calculations, although there are certain errors due primarily to the fact that the magnetic contribution to Gibbs free energy is not included in the theoretical estimation [67].

3.6. Surface energies from DFT calculations

As stated in section 1, the experimental measurement of surface energy of a solid is difficult and inaccurate, whereas DFT calculation has been a powerful approach to determine physical properties of solids, such as surface energies [11]. Ultrathin slab calculation is the most popular method to extract the surface energy of a given material [71]. However, in terms of accuracy, the quantum-size effect (QSE) [72] as a consequence of the difference of the k-meshing grids between the bulk and slab Brillouin-zones is an inevitable challenge for the surface energy calculation of alloys. Boettger [72] has proposed the linear fitting method to evaluate the bulk energy so as to eliminate the oscillation arising from the QSE of the calculated surface energies. Nevertheless, the energy difference of adjacent atomic layers is not constant in SQS supercells due to the random distribution of different atoms. Therefore, in the present work, the linear fitting method is no longer feasible, and two different DFT calculations are required to respectively evaluate the energies of the slab and the corresponding bulk lattice and the surface energy is then calculated from:

$$\gamma_s = \frac{E_s - E_{bulk}}{2A}, \tag{13}$$

where E_s and E_{bulk} are the total energies of the slab and the corresponding bulk SQS supercells, respectively, and A is the area of the plane of interest in the SQS supercell.

The energies for both the relaxed and unrelaxed surfaces without reconstruction in the alloys considered from DFT calculations are listed in table 6 and shown in figure 5. It can be observed that the surface energy increases in sequence of NiFeCu, NiCoFe, NiFeCr, and NiCoCr alloys for the (001) and (011) surfaces as shown in figures 5(a) and (b) respectively, whereas it increases in the sequence of NiFeCu, NiCoFe, NiCoCr and NiFeCr for the (111)

Table 9. Surface relaxation of the top-four interlayer spacings, $\Delta d_{12}, \Delta d_{23}, \Delta d_{34}$, and $\Delta d_{45}(\%)$ of the low-index surfaces in the alloys considered. The positive signs indicate expansion and negative signs contraction.

	NiCoCr			NiCoFe			NiFeCr			NiFeCu		
	(001)	(011)	(111)	(001)	(011)	(111)	(001)	(011)	(111)	(001)	(011)	(111)
Δd_{12}	−1.79	−8.60	−1.07	−2.99	−11.4	−1.55	1.83	−9.15	−1.03	−1.18	−3.93	−1.00
Δd_{23}	1.21	2.29	0.68	1.28	4.22	0.67	0.74	2.55	0.48	0.86	1.56	0.44
Δd_{34}	−0.28	1.77	0.31	−0.01	0.88	0.01	−0.36	1.60	0.12	−0.16	0.66	0.17
Δd_{45}	−0.13	-0.33	0.71	1.02	−0.11	0.84	−0.50	−0.46	0.16	−0.39	−0.31	0.54

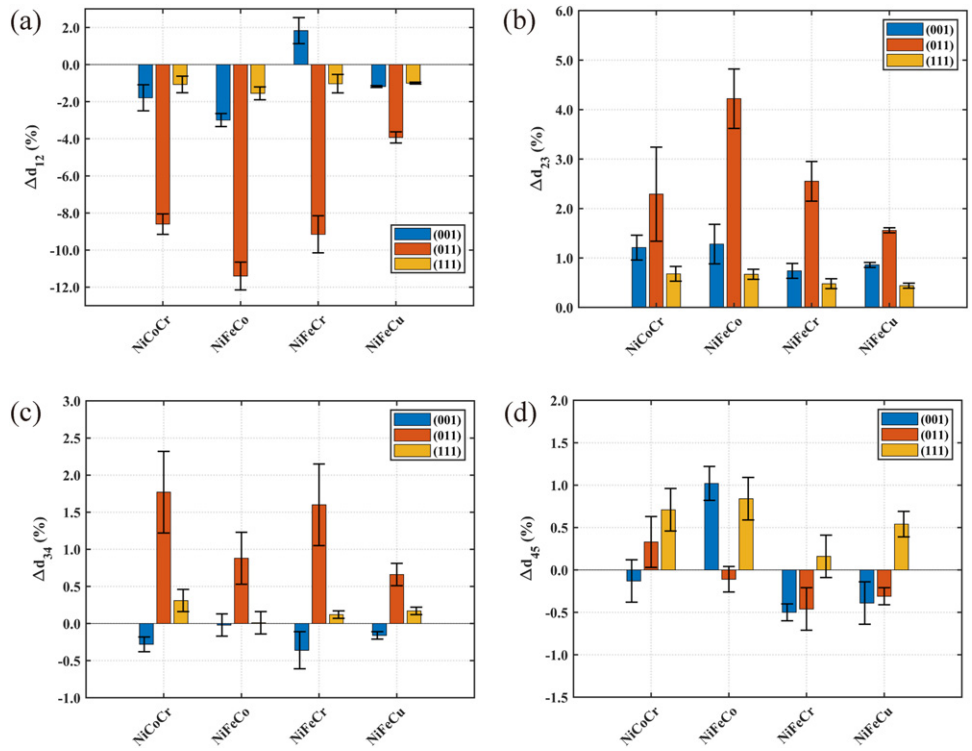

Figure 6. Surface relaxation of the top four interlayer spacings: (a) Δd_{12}; (b) Δd_{23}; (c) Δd_{34}; and (d) Δd_{45}, of the low-index surfaces in the alloys considered.

surfaces as shown in figure 5(c). The increasing trend is in good agreement with that from the BCM based on cohesive energies as discussed earlier, and the small deviation can be attributed to random effects because of the close cohesive energies for the NiFeCo, NiFeCr and NiCoCr alloys. The energy differences between unrelaxed and relaxed slabs, or equivalently, the energy differences between the halved theoretical cleavage energies and surface energies, are within about 10% with respect to the unrelaxed energies for all surfaces of the alloys considered.

3.7. Multilayer surface relaxation

Surface relaxation, as a consequence of charge redistribution when a new surface is created, is a vital characteristic of metallic surfaces. Here, we extract the average positions, due to the lattice distortion, as shown in figure 4, of the top seven layers of atoms in the direction of the slab thickness, and then calculate the relative changes in the interlayer spacings with respect to the bulk-like interlayer spacings as:

Table 10. Peak values of ELF of the four alloys.

	NiCoCr			NiCoFe			NiFeCr			NiFeCu		
Surf.	Bulk mag.	Slab mag.	Slab nonmag.	Bulk mag.	Slab mag.	Slab nonmag.	Bulk mag.	Slab mag.	Slab nonmag.	Bulk mag.	Slab mag.	Slab nonmag.
(001)	0.36	0.36	0.57	0.29	0.32	0.42	0.39	0.39	0.57	0.16	0.16	0.43
(011)	0.33	0.38	0.68	0.31	0.20	0.51	0.37	0.38	0.59	0.16	0.16	0.49
(111)	0.38	0.38	0.64	0.23	0.33	0.48	0.42	0.45	0.61	0.16	0.16	0.44

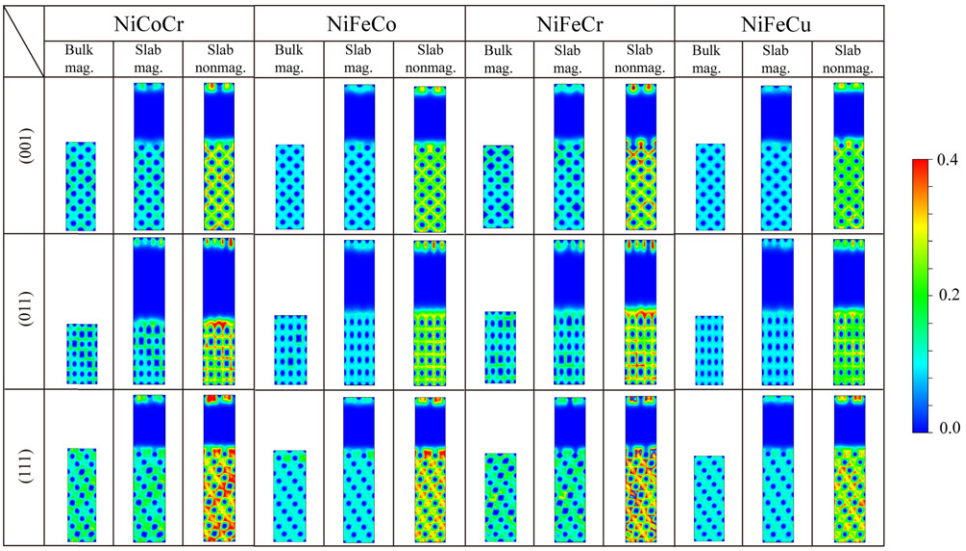

Figure 7. Two-dimensional ELF of the planes normal to the surfaces of interest for the alloys considered. The 'mag.' and 'nonmag.' denote the calculations with and without spin.

$$\Delta\overline{d}_{ij} = \frac{\overline{d}_{ij} - \overline{d}_{ij}^{\text{bulk}}}{\overline{d}_{ij}^{\text{bulk}}}, \tag{15}$$

where $\overline{d}_{ij}$ and $\overline{d}_{ij}^{\text{bulk}}$ represent the average interlayer spacing between the *i*th and *j*th layers in a slab and in the bulk respectively.

The results of the interlayer relaxation for the top five layers are summarized in table 9 and shown in figure 6. It is observed that all topmost interlayer relaxation, Δd_{12}, is in an inward contraction except for the (001) surface of NiFeCr alloy, while the second interlayer relaxation, Δd_{23}, is in outward expansion. Moreover, the extent of the interlayer relaxation on the (011) surfaces for the top-three interlayers of all the alloys considered is the most pronounced, as shown in figures 6(a)–(c). This is consistent with the prediction of the Finnis–Heine model [9], i.e. the smoothing effect is more remarkable for rougher surfaces, particularly for the topmost interlayer, which exhibits a contraction of about 4%–10% for the (011) surfaces. Specifically, the relaxation of the first and second interlayers in NiCoFe alloy is particularly significant as shown in figures 6(a) and (d). The relaxation of the top four interlayers on the (111) surfaces is very close for all the alloys as shown in figures 6(a)–(d). It is clear that the extent of interlayer relaxation gradually decays from the topmost interlayer into the interior of the slab for these alloys, as shown in table 9 and figure 6. The relaxation of the third and fourth interlayers, Δd_{34} and Δd_{45}, fluctuates around zero as shown in table 9, while that of the fifth and sixth interlayers, Δd_{56} and Δd_{67} which is not listed in table 9, is zero in our calculation, indicating that below the sixth atomic layer the interlayer spacings become bulk-like.

To gain further insights into the surface relaxation, the electron localization function (ELF) [73], which is associated with the total electron density and can be used to identify the nature of bonding in solids, such as the type and strength of bonds [74, 75], was evaluated. ELF values

can be between 0 to 1, where values of 0, 0.5 and 1 correspond to completely delocalized state, free electron-gas-like behavior, and perfect localization bonding, respectively [73]. Table 10 summaries the ELF peak values for all alloys and figure 7 compares the 2D ELF on the planes normal to the surfaces of interest of the bulk lattice and relaxed slabs. In the case of the bulk lattices in figure 7, the ELF basins are extended with the nonuniform localization rather than with the uniform localization as in pure metals, which is a consequence of the interaction between atoms with different valence electrons. When free surfaces are introduced, the local ELF values of surface atoms are close to zero for the rougher (001) and (111) surfaces and consequently, the localization regions exhibit serrations; however, the ELF values on (011) surfaces exhibit a pronounced smoothness. It demonstrates quantitatively that the smoothing effect is mainly responsible for the fact that the surface relaxation on (011) plane is the largest among the low-index surfaces studied, as shown in table 9.

Moreover, ELF analysis was carried out to obtain further insight into the magnetism effect on the surface relaxation. For the bulk lattice and relaxed slabs of these alloys, the ELF values with spin polarization considered are within about 0.2–0.4, as listed in table 10, indicating characteristics of metallic bonds. Without consideration of spin polarization, the ELF values for surface relaxation become larger than those with magnetism effect considered. For NiCoCr and NiFeCr, their peak ELF values are larger than 0.5, implying that valence electrons are localized in the solution as shown as in figure 7, and the bonding tends to be covalent. The change in the ELF values implies that magnetic moments render the type of electron interaction toward the metallic bond character. Therefore, the energies of the slabs with spin polarization considered are smaller than those without including magnetic moment contributions. In other words, the energies of the slabs are further decreased due to a decrease of d-electrons contribution caused by spin polarization during surface relaxation.

4. Conclusions

In the absence of direct experimental measurements, we have calculated the energies and relaxation of nonreconstructed low-index surfaces, i.e. (001), (011) and (111), in equiatomic multi-principal element fcc alloys NiCoCr and NiFeX (X = Cu, Co or Cr) using first principles calculations within the DFT scheme. Although the results are evidently not in perfect agreement with those obtained from theoretical estimates based on thermodynamics modeling and BCM, the trends from both methods are qualitatively consistent. With respect to surface relaxation the results show that the topmost and second interlayer spacings are in contraction, except for the (001) surface of NiFeCr alloy, and in expansion respectively, and the relaxation extent between the third and fourth interlayer spacings oscillates approximately around zero while the fifth interlayer recovers to the bulk spacing. The surface contraction on (011) plane is the most pronounced, in consistence with the smoothing effect based on d-bonding contributions for transition metals. Magnetism plays a crucial role in surface relaxation, by rendering the electron interaction toward the metallic bond character when spin polarization is taken into consideration.

Table A1. Energy (in J m^{-2}) and relaxation (in %) of the (001) surface in the NiCoCr alloy. M1 and M2 represent the cases of five independent supercells with 96 atoms and ten independent supercells with 144 atoms, respectively.

Model	$\gamma_{\text{DFT-(100)}}$	Δd_{12}	Δd_{23}	Δd_{34}	Δd_{45}
M1	2.552(±0.08)	−1.79	1.21	−0.28	−0.13
M2	2.543(±0.06)	−1.76	1.09	0.13	0.55

Acknowledgments

This research is supported by the National Natural Science Foundation of China (Nos. 11932004 and 12102069) and the Natural Science Foundation of Chongqing (No. cstc2020jcyj-bsh0073). AHWN acknowledges support from the National Key R & D Programme, Ministry of Science and Technology, China (No. 2019YFA0209900). JAE acknowledges support by the US National Science Foundation (DMR-1807708).

Data availability statement

All data that support the findings of this study are included within the article (and any supplementary files).

Appendix. Convergence tests for system size and randomness

We repeated the calculations for the (001) surface in NiCoCr alloy with more atoms (i.e. 144 in total and 12 per layer) and independent random models (ten independent SQS supercells). The results, shown in table A1, confirm that our initial setting of five independent supercells with 96 atoms each is sufficient to reproduce the surface properties of the alloy.

We also repeated the calculations for the surface relaxation within the top four and six atomic layers for the NiCoCr alloy as shown in table A2, where the fifth interlayer spacing (Δd_{56}) is found to be equal to the bulk spacing thus indicating no relaxation has occurred. The results therefore indicate that the size of the calculation used in the main text is large enough to guarantee that boundary effects are minimal. Besides, for the (100) surface in NiFeCr, we also performed similar convergence tests for the surface relaxation as those in table A1, where the relaxation within the top four, six and seven atomic layers was calculated; we found that all the first interlayer spacings are in expansion.

Table A2. Surface relaxation (in %) of the top four interlayer spacings, $\Delta d_{12}\Delta d_{23}$, Δd_{34} and Δd_{45} (%), of low-index surfaces in NiCoCr, and the (100) surface in NiFeCr. Δd_{56} and Δd_{67} are both zero for the relaxation with seven atomic layers involved.

	NiCoCr(4 layer_relax.)			NiCoCr(6 layer_relax.)			NiCoCr(7 layer_relax.)			NiFeCr		
	(001)	(011)	(111)	(001)	(011)	(111)	(001)	(011)	(111)	(001/4)	(001/6)	(001/7))
Δd_{12}	−1.72	−8.10	−1.13	−1.70	−8.45	−0.66	−1.79	−8.60	−1.07	1.02	0.75	1.83
Δd_{23}	1.17	2.11	0.58	1.23	2.31	0.53	1.21	2.29	0.68	1.11	1.26	0.74
Δd_{34}	−0.21	1.49	0.33	0.04	1.00	0.85	−0.28	1.77	0.31	−0.13	−0.23	−0.36
Δd_{45}	\	\	\	0	−0.01	−0.11	−0.13	−0.33	0.71	\	−0.07	−0.50

ORCID iDs

Wei Li https://orcid.org/0000-0003-3787-9357

References

[1] Cantor B, Chang I T H, Knight P and Vincent A J B 2004 Microstructural development in equiatomic multicomponent alloys *Mater. Sci. Eng.* A **375–77** 213–8
[2] Yeh J-W, Chen S-K, Lin S-J, Gan J-Y, Chin T-S, Shun T-T, Tsau C-H and Chang S-Y 2004 Nanostructured high-entropy alloys with multiple principal elements: novel alloy design concepts and outcomes *Adv. Eng. Mater.* **6** 299–303
[3] Diao H Y, Feng R, Dahmen K A and Liaw P K 2017 Fundamental deformation behavior in high-entropy alloys: an overview *Curr. Opin. Solid State Mater. Sci.* **21** 252–66
[4] Shi Y, Yang B and Liaw P 2017 Corrosion-resistant high-entropy alloys: a review *Metals* **7** 43
[5] Qiu Y, Thomas S, Gibson M A, Fraser H L and Birbilis N 2017 Corrosion of high entropy alloys *npj Mater. Degrad.* **1** 15
[6] Batchelor T A A, Pedersen J K, Winther S H, Castelli I E, Jacobsen K W and Rossmeisl J 2019 High-entropy alloys as a discovery platform for electrocatalysis *Joule* **3** 834–45
[7] Löffler T, Savan A, Garzón-Manjón A, Meischein M, Scheu C, Ludwig A and Schuhmann W 2019 Toward a paradigm shift in electrocatalysis using complex solid solution nanoparticles *ACS Energy Lett.* **4** 1206–14
[8] Kim H, Nam S, Roh A, Son M, Ham M-H, Kim J-H and Choi H 2019 Mechanical and electrical properties of NbMoTaW refractory high-entropy alloy thin films *Int. J. Refract. Met. Hard Mater.* **80** 286–91
[9] Methfessel M, Hennig D and Scheffler M 1992 Trends of the surface relaxations, surface energies, and work functions of the 4D transition metals *Phys. Rev.* B **46** 4816–29
[10] Singh-Miller N E and Marzari N 2009 Surface energies, work functions, and surface relaxations of low-index metallic surfaces from first principles *Phys. Rev.* B **80** 235407
[11] Vitos L, Ruban A V, Skriver H L and Kollár J 1998 The surface energy of metals *Surf. Sci.* **411** 186–202
[12] Tyson W R and Miller W A 1977 Surface free energies of solid metals: estimation from liquid surface tension measurements *Surf. Sci.* **62** 267–76
[13] Wang L, Lai K C, Huang L, Evans J W and Han Y 2020 Low-index surface energies, cleavage energies, and surface relaxations for crystalline NiAl from first-principles calculations *Surf. Sci.* **695** 121532
[14] Osei-Agyemang E and Balasubramanian G 2019 Surface oxidation mechanism of a refractory high-entropy alloy *npj Mater. Degrad.* **3** 20
[15] Ferrari A and Körmann F 2020 Surface segregation in Cr–Mn–Fe–Co–Ni high entropy alloys *Appl. Surf. Sci.* **533** 147471
[16] Li X, Li W, Irving D L, Varga L K, Vitos L and Schönecker S 2020 Ductile and brittle crack-tip response in equimolar refractory high-entropy alloys *Acta Mater.* **189** 174–87
[17] Holec D and Mayrhofer P H 2012 Surface energies of AlN allotropes from first principles *Scr. Mater.* **67** 760–2
[18] Zhang H Z and Wang S Q 2007 First-principles study of Ti_3AC_2 (A = Si, Al) (001) surfaces *Acta Mater.* **55** 4645–55
[19] Zunger A, Wei S-H, Ferreira L G and Bernard J E 1990 Special quasirandom structures *Phys. Rev. Lett.* **65** 353–6
[20] Zaddach A J, Niu C, Koch C C and Irving D L 2013 Mechanical properties and stacking fault energies of NiFeCrCoMn high-entropy alloy *JOM* **65** 1780–9
[21] Niu C, Zaddach A J, Oni A A, Sang X, Hurt J W, LeBeau J M, Koch C C and Irving D L 2015 Spin-driven ordering of Cr in the equiatomic high entropy alloy NiFeCrCo *Appl. Phys. Lett.* **106** 161906
[22] Rao S I, Akdim B, Antillon E, Woodward C, Parthasarathy T A and Senkov O N 2019 Modeling solution hardening in BCC refractory complex concentrated alloys: NbTiZr, $Nb_{1.5}TiZr_{0.5}$ and $Nb_{0.5}TiZr_{1.5}$ *Acta Mater.* **168** 222–36

[23] van de Walle A *et al* 2013 Efficient stochastic generation of special quasirandom structures *Calphad* **42** 13–8
[24] Jiang C 2009 First-principles study of ternary bcc alloys using special quasi-random structures *Acta Mater.* **57** 4716–26
[25] Gao M C, Yeh J-W, Liaw P K and Zhang Y 2016 *High-Entropy Alloys: Fundamentals and Applications* (Berlin: Springer)
[26] Kresse G and Hafner J 1993 *Ab initio* molecular dynamics for liquid metals *Phys. Rev.* B **47** 558–61
[27] Kresse G and Furthmüller J 1996 Efficient iterative schemes for *ab initio* total-energy calculations using a plane-wave basis set *Phys. Rev.* B **54** 11169–86
[28] Hacene M, Anciaux-Sedrakian A, Rozanska X, Klahr D, Guignon T and Fleurat-Lessard P 2012 Accelerating VASP electronic structure calculations using graphic processing units *J. Comput. Chem.* **33** 2581–9
[29] Hutchinson M and Widom M 2012 VASP on a GPU: application to exact-exchange calculations of the stability of elemental boron *Comput. Phys. Commun.* **183** 1422–6
[30] Kresse G and Joubert D 1999 From ultrasoft pseudopotentials to the projector augmented-wave method *Phys. Rev.* B **59** 1758–75
[31] Perdew J P, Burke K and Ernzerhof M 1996 Generalized gradient approximation made simple *Phys. Rev. Lett.* **77** 3865–8
[32] Ye Y F, Zhang Y H, He Q F, Zhuang Y, Wang S, Shi S Q, Hu A, Fan J and Yang Y 2018 Atomic-scale distorted lattice in chemically disordered equimolar complex alloys *Acta Mater.* **150** 182–94
[33] Monkhorst H J and Pack J D 1976 Special points for Brillouin-zone integrations *Phys. Rev.* B **13** 5188–92
[34] Zhang Y, Zuo T T, Tang Z, Gao M C, Dahmen K A, Liaw P K and Lu Z P 2014 Microstructures and properties of high-entropy alloys *Prog. Mater. Sci.* **61** 1–93
[35] Li W, Fan H, Tang J, Wang Q, Zhang X and El-Awady J A 2019 Effects of alloying on deformation twinning in high entropy alloys *Mater. Sci. Eng.* A **763** 138143
[36] Toda-Caraballo I, Wróbel J S, Dudarev S L, Nguyen-Manh D and Rivera-Díaz-del-Castillo P E J 2015 Interatomic spacing distribution in multicomponent alloys *Acta Mater.* **97** 156–69
[37] Tyson W R 1975 Surface energies of solid metals *Can. Metall. Q.* **14** 307–14
[38] Miller W A and Chadwick G A 1967 On the magnitude of the solid/liquid interfacial energy of pure metals and its relation to grain boundary melting *Acta Metall.* **15** 607–14
[39] Arslan H and Dogan A 2019 Determination of surface tension of liquid ternary Ni–Cu–Fe and sub-binary alloys *Phil. Mag.* **99** 1206–24
[40] Tanaka T and Iida T 1994 Application of a thermodynamic database to the calculation of surface tension for iron-base liquid alloys *Steel Res.* **65** 21–8
[41] Tanaka T, Hack K and Hara S 1999 Use of thermodynamic data to determine surface tension and viscosity of metallic alloys *MRS Bull.* **24** 45–51
[42] Costa C, Delsante S, Borzone G, Zivkovic D and Novakovic R 2014 Thermodynamic and surface properties of liquid Co–Cr–Ni alloys *J. Chem. Thermodyn.* **69** 73–84
[43] Brillo J, Egry I and Matsushita T 2006 Density and surface tension of liquid ternary Ni–Cu–Fe alloys *Int. J. Thermophys.* **27** 1778–91
[44] Guillermet A F 1988 Assessing the thermodynamics of the Fe–Co–Ni system using a calphad predictive technique *Calphad* **13** 1–22
[45] Xiong W, Hedström P, Selleby M, Odqvist J, Thuvander M and Chen Q 2011 An improved thermodynamic modeling of the Fe–Cr system down to zero kelvin coupled with key experiments *Calphad* **35** 355–66
[46] Chou K-C 1995 A general solution model for predicting ternary thermodynamic properties *Calphad* **19** 315–25
[47] Zhang G-H and Chou K-C 2010 General formalism for new generation geometrical model: application to the thermodynamics of liquid mixtures *J. Solut. Chem.* **39** 1200–12
[48] Egry I, Brillo J and Matsushita T 2005 Thermophysical properties of liquid Cu–Fe–Ni alloys *Mater. Sci. Eng.* A **413–414** 460–4
[49] Hebbache M and Zemzemi M 2004 *Ab initio* study of high-pressure behavior of a low compressibility metal and a hard material: osmium and diamond *Phys. Rev.* B **70** 224107
[50] Schimka L, Gaudoin R, Klimeš J, Marsman M and Kresse G 2013 Lattice constants and cohesive energies of alkali, alkaline-earth, and transition metals: random phase approximation and density functional theory results *Phys. Rev.* B **87** 214102
[51] Kittel C 2007 *Introduction to Solid State Shysics* 7th ed (New York: Wiley)

[52] Chen B, Penwell D and Kruger M B 2000 The compressibility of nanocrystalline nickel *Solid State Commun.* **115** 191–4
[53] Mishin Y, Mehl M J and Papaconstantopoulos D A 2002 Embedded-atom potential for B2–NiAl *Phys. Rev.* B **65** 224114
[54] Schimka L, Harl J and Kresse G 2011 Improved hybrid functional for solids: the HSEsol functional *J. Chem. Phys.* **134** 024116
[55] Haas P, Tran F and Blaha P 2009 Calculation of the lattice constant of solids with semilocal functionals *Phys. Rev.* B **79** 085104
[56] Johnson D F, Jiang D E and Carter E A 2007 Structure, magnetism, and adhesion at Cr/Fe interfaces from density functional theory *Surf. Sci.* **601** 699–705
[57] Kübler J 1980 Spin-density functional calculations for chromium *J. Magn. Magn. Mater.* **20** 277–84
[58] Cottenier S, Vries B D, Meersschaut J and Rots M 2002 What density-functional theory can tell us about the spin-density wave in Cr *J. Phys.: Condens. Matter.* **14** 3275–83
[59] de la Peña O'Shea V A, Moreira I de P R, Roldán A and Illas F 2010 Electronic and magnetic structure of bulk cobalt: the α, β, and ε-phases from density functional theory calculations *J. Chem. Phys.* **133** 024701
[60] Jin K, Gao Y F and Bei H 2017 Intrinsic properties and strengthening mechanism of monocrystalline Ni-containing ternary concentrated solid solutions *Mater. Sci. Eng.* A **695** 74–9
[61] Tian F, Varga L K, Chen N, Shen J and Vitos L 2015 Empirical design of single phase high-entropy alloys with high hardness *Intermetallics* **58** 1–6
[62] Pereira R, Camargo P C, de Oliveira A J A and Pereira E C 2017 Modulation of the morphology, microstructural and magnetic properties on electrodeposited NiFeCu alloys *Surf. Coat. Technol.* **311** 274–81
[63] Zhang R, Zhao S, Ding J, Chong Y, Jia T, Ophus C, Asta M, Ritchie R O and Minor A M 2020 Short-range order and its impact on the CrCoNi medium-entropy alloy *Nature* **581** 283–7
[64] Haiss W 2001 Surface stress of clean and adsorbate-covered solids *Rep. Prog. Phys.* **64** 591–648
[65] Zhao M, Zheng W, Li J, Wen Z, Gu M and Sun C Q 2007 Atomistic origin, temperature dependence, and responsibilities of surface energetics: an extended broken-bond rule *Phys. Rev.* B **75** 085427
[66] Mezey L Z and Giber J 1982 The surface free energies of solid chemical elements: calculation from internal free enthalpies of atomization *Japan. J. Appl. Phys.* **21** 1569–71
[67] Aldén M, Skriver H L, Mirbt S and Johansson B 1994 Surface energy and magnetism of the 3D metals *Surf. Sci.* **315** 157–72
[68] Guo S 2015 Phase selection rules for cast high entropy alloys: an overview *Mater. Sci. Technol.* **31** 1223–30
[69] Miracle D B and Senkov O N 2017 A critical review of high entropy alloys and related concepts *Acta Mater.* **122** 448–511
[70] Allen B C 1972 The interfacial free energies of solid chromium, molybdenum and tungsten *J. Less Common Met.* **29** 263–82
[71] Boettger J C 1994 Nonconvergence of surface energies obtained from thin-film calculations *Phys. Rev.* B **49** 16798–800
[72] Boettger J C 1996 Persistent quantum-size effect in aluminum films up to twelve atoms thick *Phys. Rev.* B **53** 13133–7
[73] Becke A D and Edgecombe K E 1990 A simple measure of electron localization in atomic and molecular systems *J. Chem. Phys.* **92** 5397–403
[74] Savin A, Nesper R, Wengert S and Fässler T F 1997 ELF: the electron localization function *Angew. Chem., Int. Ed.* **36** 1808–32
[75] Koumpouras K and Larsson J A 2020 Distinguishing between chemical bonding and physical binding using electron localization function (ELF) *J. Phys.: Condens. Matter.* **32** 315502